Vorticity production in shock diffraction

doi: 10.1017/S0022112002003403

J. Fluid Mech. (2003), *vol.* 478, *pp.* 237–256.
DOI: 10.1017/S0022112002003403 Printed in the United Kingdom

Vorticity production in shock diffraction

By M. SUN AND K. TAKAYAMA

Shock Wave Research Center, Institute of Fluid Science, Tohoku University, Katahira 2-1-1, Aoba, Sendai 980-8577, Japan

(Received 17 September 2001 and in revised form 15 October 2002)

The production of vorticity or circulation production in shock wave diffraction over sharp convex corners has been numerically simulated and quantified. The corner angle is varied from 5° to 180°. Total vorticity is represented by the circulation, which is evaluated by integrating the velocity along a path enclosing the perturbed region behind a diffracting shock wave. The increase of circulation in unit time, or the rate of circulation production, depends on the shock strength and wall angle if the effects of viscosity and heat conductivity are neglected. The rate of vorticity production is determined by using a solution-adaptive code, which solves the Euler equations. It is shown that the rate of vorticity production is independent of the computational mesh and numerical scheme by comparing solutions from two different codes. It is found that larger wall angles always enhance the vorticity production. The vorticity production increases sharply when the corner angle is varied from 15° to 45°. However, for corner angles over 90°, the rate of vorticity production hardly increases and reaches to a constant value. Strong shock waves produce vorticity faster in general, except when the slipstream originating from the shallow corner attaches to the downstream wall. It is found that the vorticity produced by the slipstream represents a large proportion of the total vorticity. The slipstream is therefore a more important source of vorticity than baroclinic effects in shock diffraction.

1. Introduction

The formation of a spiral vortex a few microseconds after shock wave diffraction over a convex corner is one of the most rapid and intricate flow processes in nature. A schematic of shock diffraction over a convex corner is shown in figure 1. The production of vortices in this process was observed many decades ago (Howard & Matthews 1956; Rott 1956; Skews 1967; Emrich & Reichenbach 1969, etc.). The starting processes when a shock wave propagates over solid boundaries with a corner, as in the case of a blast wave interacting with an airplane wing or the starting shock wave in a hypersonic shock tunnel, are some typical situations where such flows can be observed. A sharp corner, either in two-dimensional or axisymmetric flows, has also been used as a vortex generator in shock tube experiments. However, very little work has been carried out in order to measure and analyse the strength of the vortices produced.

In the first volume of this Journal, Rott (1956) proposed, in the case of weak shock waves, a single vortex model using the acoustic approximation, and derived a relation to estimate the flow circulation. This relation includes an unknown parameter, which has to be experimentally determined. He noticed that his theory disagreed with the experiments conducted by Howard & Matthews (1956), especially for large corner

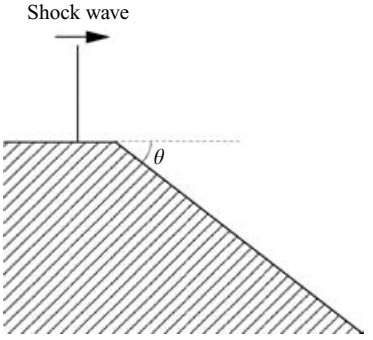

FIGURE 1. Schematic of shock diffraction over a convex corner.

angles. So he eventually abandoned his single vortex model, and realized that the vortex sheet or the slipstream starting from the corner instead of a single vortex should be analysed, and proposed a formula which could evaluate the production of vorticity, in a form slightly different from his original one,

$$\frac{\Gamma}{t} = \tfrac{1}{2}U_1^2 - \tfrac{1}{2}U_2^2, \tag{1.1}$$

where U_1 and U_2 are flow velocities on each side of the slipstream, but he could not go further using incompressible theory. In this paper we will show it is possible to evaluate the velocities using the theory of compressible flows.

Skews (1967) investigated, by using the schlieren method, the perturbed region behind a diffracting shock wave over various convex corners. The vortex angle and velocity were measured for a wide range of shock strength. He found that the vortex angle and velocity approach a limit for wall angles greater than 105°. However, no quantitative vortex strength was reported.

Evans & Bloor (1977) simulated a vortex sheet initiated from a knife edge situated in a duct using the method of vortex discretization. The rate of vorticity shedding described by (1.1) was used to implement their method. The shape of a vortex spiral and the flow around it were well represented by the method, but they found a discrepancy of 20%–30% between their experimental and theoretical vortex roll-up rates. Again vortex strength was not measured.

The flow around a corner may become locally supersonic for incident shock Mach number greater than 1.33 ± 0.01 in air (Sun & Takayama 1997), and in such cases the incompressible theory becomes a poor approximation of shock diffraction phenomena. A benchmark test of shock diffraction over a 90° corner performed during the 18th International Symposium on Shock Waves by Takayama & Inoue (1991) shows that numerical simulation can represent very well the diffracting shock wave, expansion waves and the main vortex. Many authors (e.g. Hillier 1991; Sivier *et al.* 1992) have shown that using the Euler equations it is possible to force flow separation near the corners, and to accurately capture the slipstream development and the vortex formation. However, the vorticity generation was only described, but not quantified.

The present work aims to quantify vorticity production, or the strength of the vortex that appears in shock diffraction over a wide range of wall angles by numerically solving the compressible Euler equations. Attention is also paid to the mechanism of vorticity production. It is very common for the vorticity to be ascribed entirely to the baroclinic effects. The present quantitative data show that the vorticity produced

by the slipstream represents a large portion of the total vorticity, and the baroclinic effects are negligible in shock diffraction.

The paper is organized as follows. Section 2 introduces the solution-adaptive Eulerian solver used in this study. Section 3 is devoted to the definition of vorticity strength and the method to evaluate it numerically. In § 4, the vorticity production for a wide range of convex complex angles and shock strength is tabulated. The effect of wall angle and incident shock strength on the vorticity production is discussed in § 4.1 and § 4.2. An analytical model is proposed to estimate the vorticity produced by slipstream in § 4.3. A few remarks on the mechanism of vorticity production and viscous effects are given in § 4.4.

2. Numerical simulation

Experimentally, it is not easy to measure vorticity in highly unsteady flows with shock waves. Although some techniques have recently been developed and applied to measure the velocity distribution in high-speed compressible flows, the accuracy and the resolution of these techniques are still not good enough for the quantitative analysis of vorticity. The present work will numerically analyse the vorticity production. The reliability of numerical solutions of velocity is validated by comparing the density distribution or density derivatives with experimental photographs taken by well-developed optical techniques.

For weak shock waves at room temperature and pressure, any test gas can be considered as a perfect gas, even if viscous effects are taken into account, and the equation of state is written as

$$p = \rho R T, \tag{2.1}$$

where R is the universal gas constant divided by the molecular mass of the gas. The perfect-gas law is accurate to $\pm 10\%$ in the range $1.8 \leqslant T/T_{crit} \leqslant 15$ (see White 1974), where T_{crit} is the temperature at the critical point. For air, this temperature range is $240 \sim 2000$ K. As a direct consequence of the perfect-gas law the internal energy becomes, for $\gamma = 1.4$,

$$\rho e = \frac{p}{\gamma - 1}. \tag{2.2}$$

The two-dimensional Euler equations coupled with the equation of state (2.1) and internal energy (2.2) are numerically solved for convex corners of 5°, and 15°–180° in steps of 15° for a total of 13 wall angles. A solution-adaptive flow solver using unstructured quadrilateral meshes developed by Sun (1998) is used. The solver uses an initial unstructured quadrilateral mesh that covers the whole computational domain. Each corner is represented by an unstructured mesh. Thirteen meshes are used, one for each corner, and four of them are shown in figure 2. In the computation, the solver automatically refines the mesh cells in and around flow regions such as a shock wave, vortex and slipstream, and removes the unnecessary refined cells when these features are no longer observed in the flow.

The Euler equations are solved by the finite volume method. The change of conservative quantities in each quadrilateral cell is equal to the summation of fluxes through four interfaces. The solver contains two schemes, centred and upwind schemes, to calculate the fluxes. Both schemes are second-order accurate in time and space. The centred scheme is based on the predictor–corrector Lax–Wendroff scheme, and additional artificial viscosity is added to suppress possible oscillations (Sun 1998; Sun & Takayama 1999). The upwind scheme is the MUSCL-Hancock

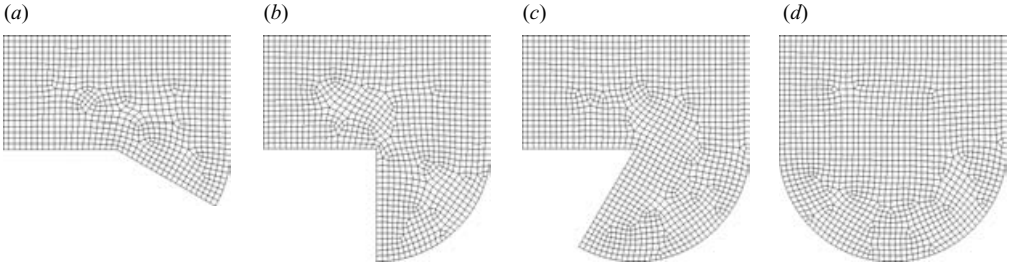

FIGURE 2. Initial unstructured quadrilateral meshes: (*a*) $\theta = 30^\circ$; (*b*) $\theta = 90^\circ$; (*c*) $\theta = 120^\circ$; (*d*) $\theta = 180^\circ$.

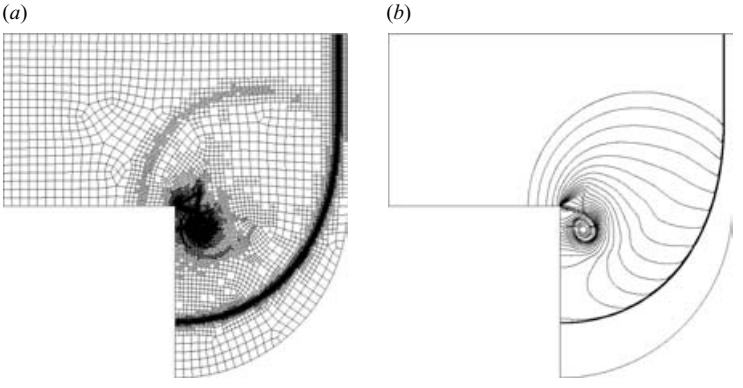

FIGURE 3. An example of solution-adaptive mesh for the 90° corner and incident shock Mach number 1.6: (*a*) unstructured quadrilateral cells with 5-level refinement; (*b*) corresponding density contours.

scheme (see Toro 1999). The minmod limiter is used to flatten slopes of primitive variables, and the fluxes through interfaces are determined by solving the HLLC approximate Riemann problem. The solver selects one of the two solutions given by the schemes, or even a solution between the two solutions in order to prevent possible negative pressures around sharp corners and irregular cells. An example of the solution-adaptive mesh is shown in figure 3(*a*). Fine cells are efficiently distributed around important flow features that can be seen in the corresponding density contours shown in figure 3(*b*). The finest mesh is approximately equivalent to a 1200×1200 uniform mesh, and numerical results in this paper are obtained using this resolution or even higher.

3. Definition of vortex strength in shock diffraction

The strength of a vortex, in a domain S enclosed by contour L, can be represented by circulation Γ, which is the summation of vorticity ω in the domain,

$$\Gamma = \int_S \omega \, \mathrm{d}s = \int_L \boldsymbol{u} \cdot \mathrm{d}l. \tag{3.1}$$

The integral contour or path L is taken along the boundary that exactly encloses the perturbed region behind a diffracting shock wave. In strict sense, it is not

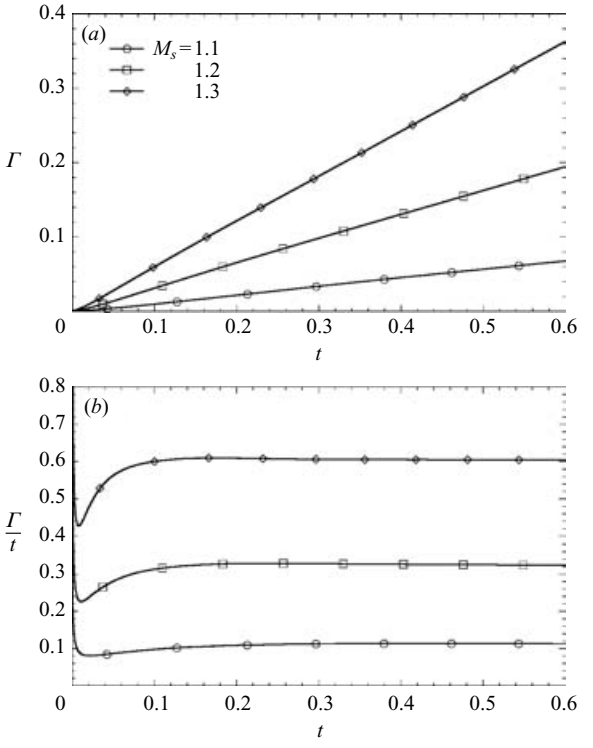

FIGURE 4. Time history of Γ and Γ/t for $\theta = 75°$: (*a*) circulation, Γ; (*b*) convergence of the rate of circulation production, Γ/t.

appropriate to apply the Green theorem in the relation (3.1) because there are velocity discontinuities in the region. Therefore, in the numerical calculation, we directly adopt

$$\Gamma = \int_L \boldsymbol{u} \cdot \mathrm{d}l \tag{3.2}$$

to represent the strength of the vortex produced by shock diffraction. In a practical evaluation, the integral is calculated along the boundary of the whole computational domain to avoid the ambiguity in determining the perturbed region in the numerical results. Since unperturbed flow regions are uniform, their contribution to the integral is zero only if the inlet is parallel to the incident shock front and there is no wave reflection from outside boundaries.

The integral is numerically evaluated by using the trapezoidal rule. The integral path along the boundary is split into the cell faces that form the computational domain, and a separate approximating linear function is used to integrate the tangential velocity on each of the cell faces. Figure 4(*a*) gives the integrated data for incident shock wave Mach numbers of $M_s = 1.1$, 1.2 and 1.3 diffracting over a 75° corner. The circulation is calculated at every time step, and about 2500 data points are recorded along each line. The time instant when the incident shock wave arrives at the corner is considered to be $t = 0$, and it starts diffracting with the elapse of time t. It is seen that the circulation increases linearly with time for all three shock strengths, except

in the region near the origin. This is also observed in shock diffraction over other wall angles.

The linear increase of circulation with time is due to the self-similar property of the Eulerian solutions. If viscosity and heat conductivity are neglected, shock wave diffraction is self-similar, that is, physical variables (pressure, density and velocity), can be expressed as functions of $(x/t, y/t)$. In (3.2), the integral path enclosing the perturbed region expands linearly with time, and the velocity values along the path remain unchanged because of self-similarity, which implies that the circulation must increase linearly with time as the integral path does. Therefore, a better quantity to characterize the vorticity production in shock production is the ratio of circulation to time, Γ/t, which is referred to as the rate of circulation production in this paper.

The rate of circulation production is related to the incident shock Mach number M_s, the diffraction angle, and gas properties. For a given gas, the ratio Γ/t can be uniquely determined for given shock wave strength and wall angle,

$$\frac{\Gamma}{t} = f(M_s, \theta), \tag{3.3}$$

where θ is the wall angle. Figure 4(b) shows the rate of circulation production under the same conditions as figure 4(a). Sharp peaks that appear near the origin are due to the very small value in the denominator. The three curves soon reach a different constant value, 0.112, 0.324 and 0.605 for $M_s = 1.1$, 1.2 and 1.3 respectively. These values should be invariants of the Euler equations in shock diffraction. A more accurate method to obtain the rate of circulation production is to calculate the time derivative of circulation from data like those shown in figure 4(a). Two circulation values, Γ_1 and Γ_2, are selected with a large time interval Δt between them; then

$$\frac{\Gamma}{t} = \frac{\Gamma_2 - \Gamma_1}{\Delta t}. \tag{3.4}$$

The first value is set for $t = 0.1$ in most computations in order to cut off the data near the origin that are in the very early stage of initiation, where artificial viscosity cannot be neglected. The second value is chosen very close to the final available data so that Δt becomes sufficiently large. This method gives rates of circulation production of 0.115, 0.326 and 0.606, which agree well with the values above. The rate of vorticity production converges rapidly for stronger shock waves, and the accuracy is therefore better.

We compared the values of Γ/t obtained by using the upwind and the centred schemes, and found their difference to be negligible. This indicates that the data obtained are independent of numerical scheme. We further investigated the possible influence of grid mesh by comparing with another solution-adaptive solver using triangles. The solver, developed by Voinovich (1993), is based on a second-order Godunov-type scheme using a TVD limiter and solving the exact Riemann problem to determine fluxes. Figure 5 gives a comparison of convergence histories obtained by these two codes for a $M_s = 1.5$ shock diffracting over a 90° corner. It is seen that these solutions converge to nearly an identical value, 1.36, within $\pm 1\%$.

It is emphasized here that the two codes are based on different schemes and meshes, and corresponding intrinsic artificial dissipations are also different. This is why the two curves disagree with each other at early stages. Since solutions of the Euler equations must be self-similar, and since physical viscosity is not taken into account in the numerical codes, the numerical data for a short time after shock diffraction are neither the solution of the Euler equations nor that of Navier–Stokes

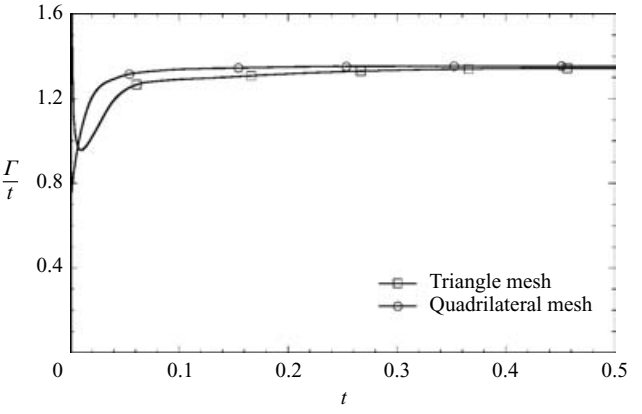

FIGURE 5. Comparison of convergence histories of two different adaptive codes.

equations. Therefore, data obtained near the origin are not reliable. The curves shown in figure 4(*b*) and figure 5 just represent the numerical evolution due to artificial viscosity, and are not physical. Only the asymptotic value is an invariant of the Euler equations. In shock diffraction any solution of the Euler equations that deviates from linear self-similarity is non-physical.

Note that all the data of circulation production recorded in the paper are dimensionless values. Since the rate has the dimension of the square of the velocity, one may obtain dimensional data by multiplying the dimensionless value with the square of the characteristic velocity,

$$\frac{\Gamma'}{t'} = RT_0 \frac{\Gamma}{t}, \tag{3.5}$$

where T_0 is the temperature in front of incident shock waves. It is seen that the rate of circulation production is proportional to the temperature in front of shock waves.

4. Results and discussion

All the data on the rate of circulation production obtained from numerical simulations are listed in table 1. To obtain one datum in the table, the Euler equations are solved for around 2500 steps. We have obtained one value from (3.4) and another is directly calculated at the last step. These two values are very close to each other for high Mach number ($M_s \geqslant 1.2$) and large wall angles ($\theta \geqslant 75^\circ$), and the difference between them is below 1%. In other regions where solutions are more difficult to converge, if three effective digits are shown, the difference is within 3%; otherwise the difference may increase up to 8%. Only the values calculated from gradient formula (3.4) are listed in the table.

The diffraction of the shock wave around various convex corners visualized using double-exposure holographic interferometry is shown in figure 6. The fringes correspond to constant relative density contours. Experiments were conducted using a 60 mm × 150 mm diaphragmless shock tube (Yang 1995) in the Shock Wave Research Center, Tohoku University. The double-exposure holographic interferometry was carried out using a Q-switched ruby laser with 25 ns pulse duration. The height of shock tube is 60 mm, and the light path is 150 mm. The initial pressures in front of the

$\theta \backslash M_s$	1.05	1.1	1.2	1.3	1.4	1.5	1.6	1.7	3.0	5.0
5°	0.00011	0.00049	0.0023	0.0058	0.0107	0.0164	0.0239	0.0343	0.24	0.85
15°	0.00029	0.0013	0.011	0.028	0.097	0.19	0.193	0.211	0.66	2.4
30°	0.0034	0.0015	0.095	0.288	0.519	0.84	0.758	0.762	1.65	5.7
45°	0.015	0.054	0.214	0.438	0.719	1.05	1.43	1.75	3.32	10.4
60°	0.030	0.092	0.278	0.535	0.828	1.19	1.54	1.94	6.49	18.4
75°	0.0401	0.115	0.326	0.606	0.933	1.30	1.67	2.09	8.98	26.4
90°	0.0488	0.134	0.364	0.657	0.990	1.36	1.74	2.15	9.16	27.3
105°	0.0547	0.145	0.386	0.681	1.019	1.39	1.77	2.175	9.25	27.7
120°	0.0601	0.156	0.402	0.700	1.036	1.40	1.79	2.187	9.29	27.8
135°	0.0644	0.164	0.413	0.711	1.045	1.408	1.791	2.193	9.31	27.9
150°	0.0678	0.168	0.419	0.716	1.050	1.411	1.791	2.193	9.31	27.9
165°	0.0702	0.172	0.422	0.719	1.051	1.411	1.793	2.193	9.31	27.9
180°	0.0715	0.174	0.423	0.718	1.050	1.410	1.793	2.195	9.31	27.9

TABLE 1. The rate of circulation production for $\gamma = 1.4$ in shock diffraction calculated from (3.4). The data are normalized by RT_0, where R is the universal gas constant divided by the molecular weight of gas and T_0 is the temperature in front of incident shock wave.

shock wave were 25 kPa and 40 kPa for $M_s = 1.50$ and 1.40, respectively. The test gas was nitrogen at room temperature of 298 ± 2 K in all experiments.

4.1. *The effect of wall angle*

A number of experimental and numerical results are given in figures 6 and 7. The flows near the corner with small angles are rather simple as shown in figures 6(*a*) and 7(*a*). The expansion waves are generated from the corner and the shock front starts to bend from where these expansion waves interact with the shock wave. Neither clearly defined vortices nor slipstreams are visible around the corner. For the 30° corner, a vortex appears as shown in figures 6(*b*) and 7(*b*). The shape of the vortex is stretched due to strong interaction with the downstream wall. The vortex grows quickly with the increase of wall angle from 30° to 60° (figure 7*b–d*). However, when the wall angle is greater than 90°, the vortex hardly changes its shape (figure 6*d–f*).

By comparing the numerical and experimental results, it is clear that the numerical simulation can reproduce the diffracted shock front, reflected expansion waves, and even the shape of vortex with a reasonable degree of accuracy. The rate of circulation production defined in § 3 is calculated. All the data for shock Mach number $M_s = 1.05$, and 1.1–1.7 in steps of 0.1 are plotted in figure 8. It is seen that the rate of vorticity shedding always increases with the wall angle for a given shock Mach number. This can be explained qualitatively: a large wall angle allows a large space for vorticity production. The vorticity production increases sharply near a wall angle of 30°. For instance, the vorticity increases by approximately four times when the wall angle changes from 15° to 45° for $M_s = 1.5$. However, for wall angles over 90°, the vorticity production hardly changes, and all curves tend to approach their corresponding constant values.

From experimental photos, some tiny secondary vortices that lie between the corner and the main vortex are observable (figure 6*d–f*). The main vortex is generally much larger than the secondary vortices. In numerical simulations, secondary vortices have not been detected in Eulerian solutions, but can be seen in the solution of the Navier–Stokes equations. The viscosity plays a role in the formation and evolution of these secondary vortices, so that the mechanisms of vortex formation for the main vortex and the secondary vortices should be different. The secondary vortices are formed

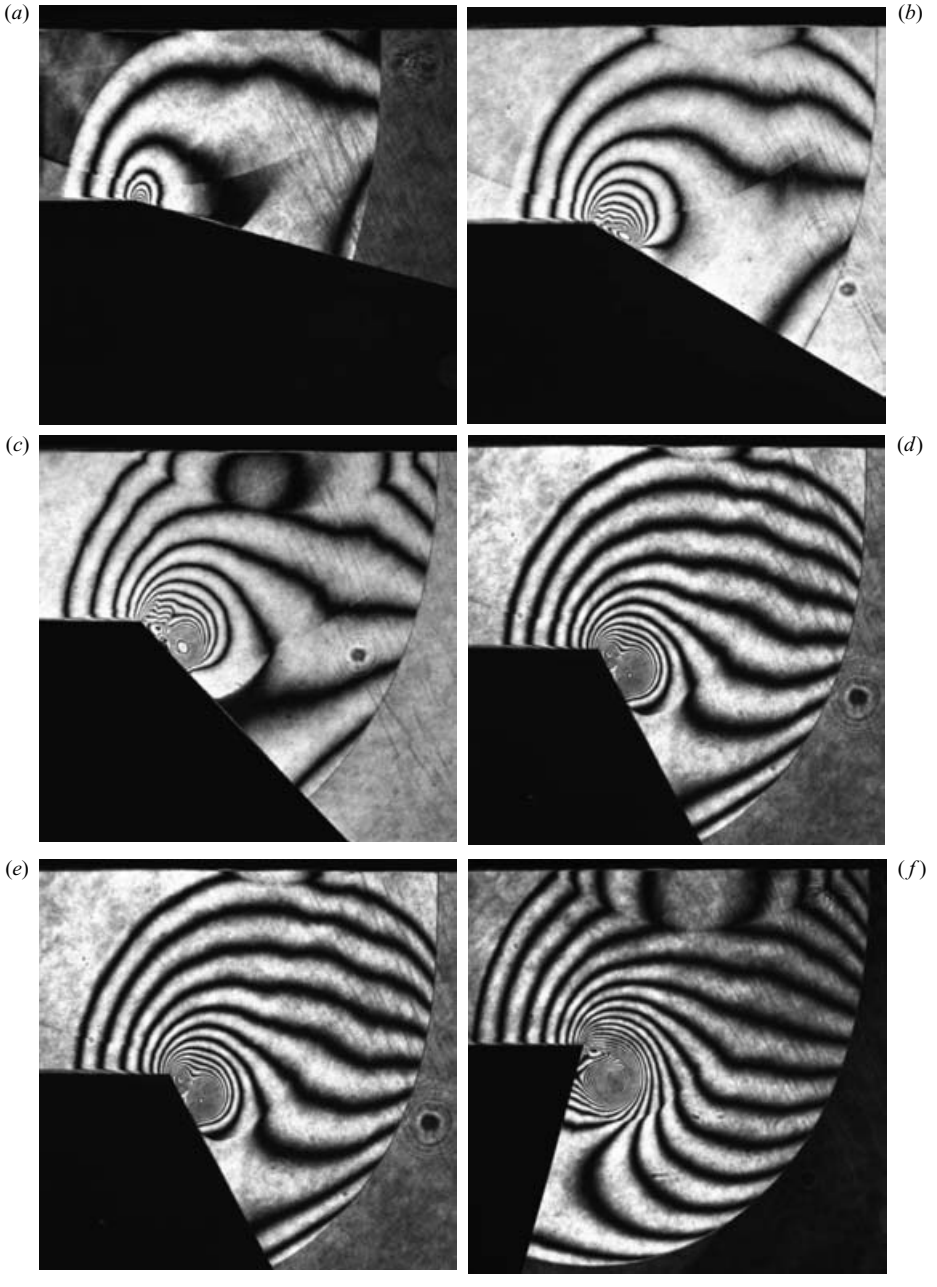

FIGURE 6. Results of shock diffraction in nitrogen taken by holographic interferometry: (*a*) $\theta = 15°$, $M_s = 1.51$; (*b*) $\theta = 30°$, $M_s = 1.50$; (*c*) $\theta = 45°$, $M_s = 1.50$; (*d*) $\theta = 60°$, $M_s = 1.40$; (*e*) $\theta = 90°$, $M_s = 1.40$; (*f*) $\theta = 105°$, $M_s = 1.40$.

due to the separation of the boundary layer on the downstream wall. This paper focuses on the analysis of the main vortex, and results for the secondary vortices will be documented in a separate paper.

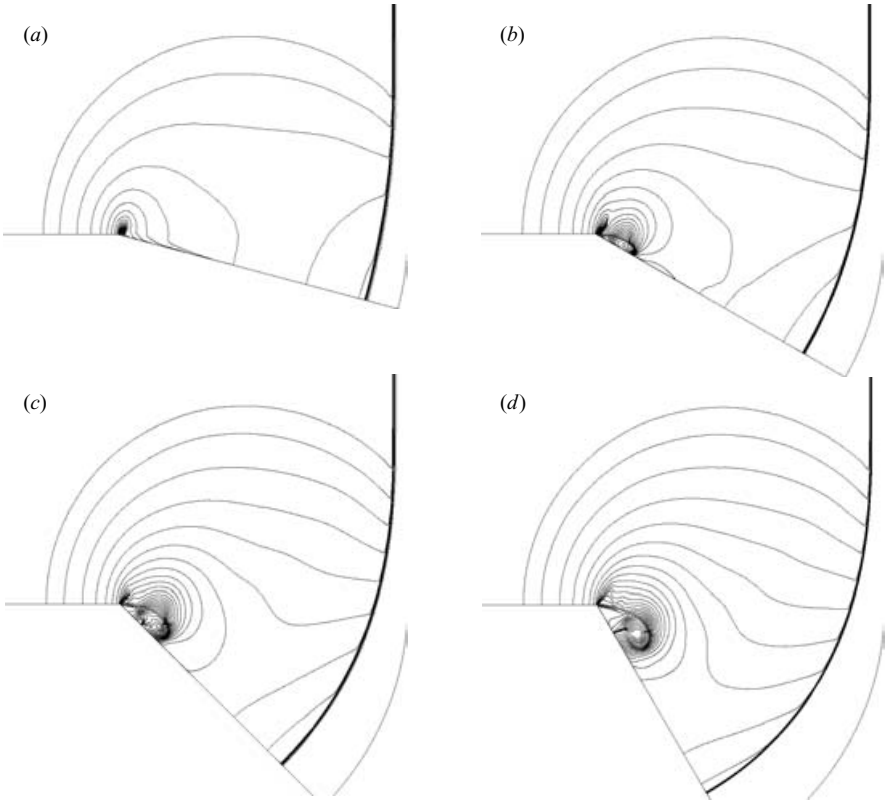

FIGURE 7. Numerical density contours for $M_s = 1.5$: (*a*) $\theta = 15°$; (*b*) $\theta = 30°$; (*c*) $\theta = 45°$; (*d*) $\theta = 60°$.

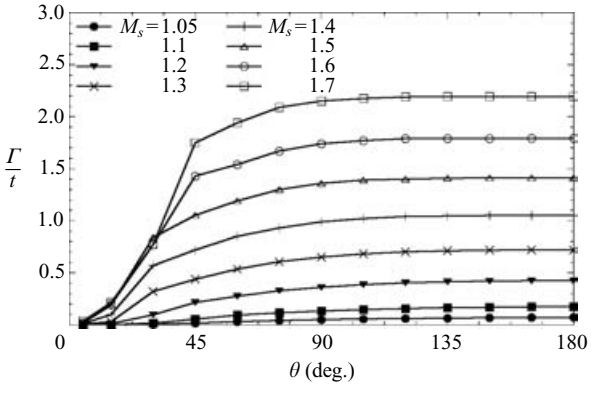

FIGURE 8. Effect of wall angle on the rate of circulation production.

4.2. *The effect of incident shock strength*

The effect of shock strength on the rate of vorticity production is investigated by changing incident shock Mach number M_s. Figures 9 and 10 show a shock diffracting over a 135° corner for the shock Mach numbers 1.23, 1.6, 2.43 and 3.0, which

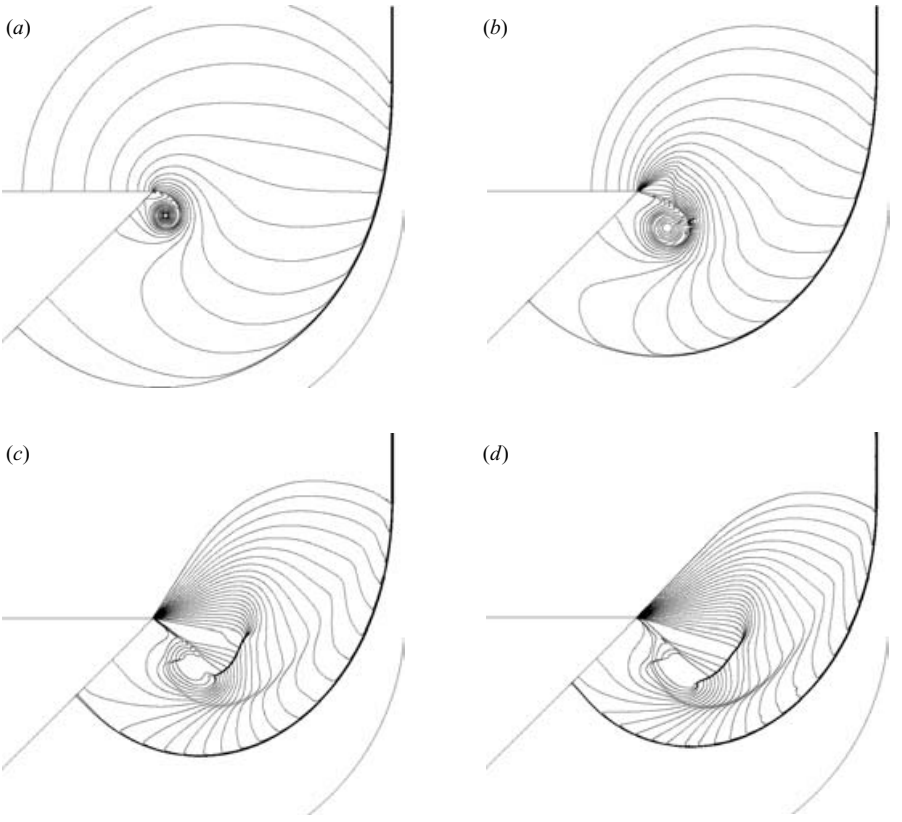

FIGURE 9. Shock diffraction over a 135° corner, density contours: (*a*) $M_s = 1.23$; (*b*) $M_s = 1.6$; (*c*) $M_s = 2.43$; (*d*) $M_s = 3.0$.

are the same conditions as those of colour schlieren photographs taken by Skews (1967). The wave structures and vortex shape agree very well with the experimental photographs. For weak shock waves, a vortex spiral is formed downstream of the corner as seen in figure 10(*a*) and 10(*b*), and the vortex is nearly circular and fairly well defined. The vortex spreads for $M_s = 1.6$, and this can be recognized by comparing the locations of the vortex centre in the two figures. For strong shock waves, the secondary shock wave penetrates into the vortex, and distorts it. This interaction even involves the contact surface and the lower end of the secondary shock wave.

It should be noted that experimental photos show that the vortex regions may become turbulent for strong shock waves (Skews 1967), and the vortex appears rather diffuse and the position of its centre can no longer be determined clearly. Our preliminary study indicates that the vortex can be turbulent even for $M_s = 1.5$. The vorticity distribution for strong shock waves shown in figure 10(*c*, *d*) should be smeared in reality due to strong turbulent dissipation.

Figure 11 gives the rate of circulation production as a function of shock Mach number up to $M_s = 1.7$. Data for stronger shocks ($M_s = 3, 5$) are listed in table 1. The rate basically increases with shock strength, and it increases much faster for wall angles greater than 45°. There is a peak for the 30° corner at $M_s = 1.5$, and the

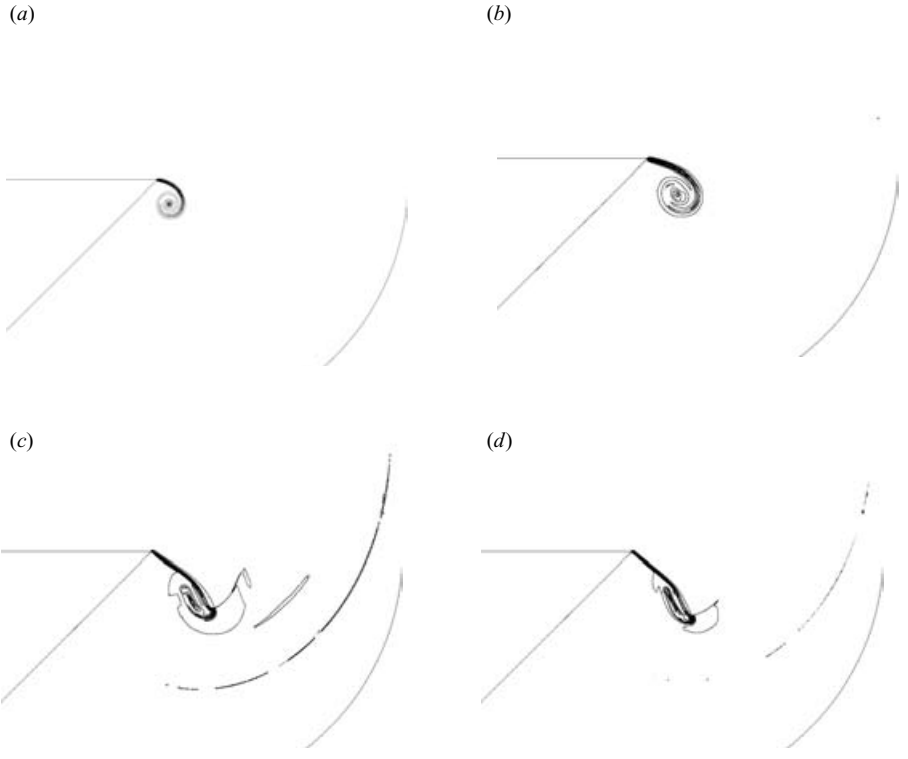

FIGURE 10. Shock diffraction over a 135° corner, vorticity contours: (*a*) $M_s = 1.23$; (*b*) $M_s = 1.6$; (*c*) $M_s = 2.43$; (*d*) $M_s = 3.0$.

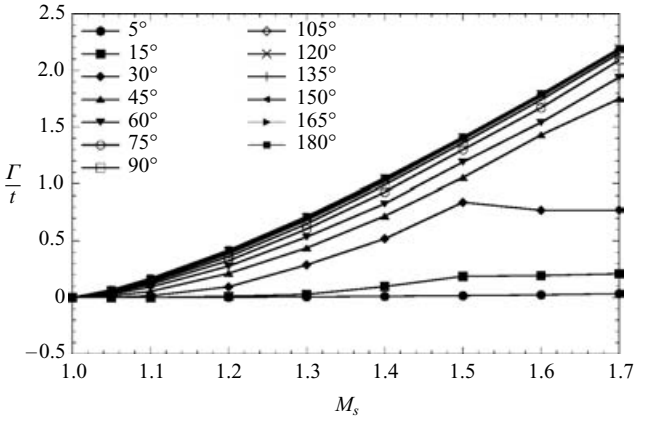

FIGURE 11. Effect of incident shock strength on the rate of circulation production.

vorticity production decreases for stronger shock waves. However, for the 45° corner, it increases monotonically with the shock strength. To clarify this difference, numerical results for these two corners are displayed in figure 12 for $M_s = 1.4$ and $M_s = 1.6$. Flow patterns around the two corners are very similar for $M_s = 1.4$: a vortex spiral

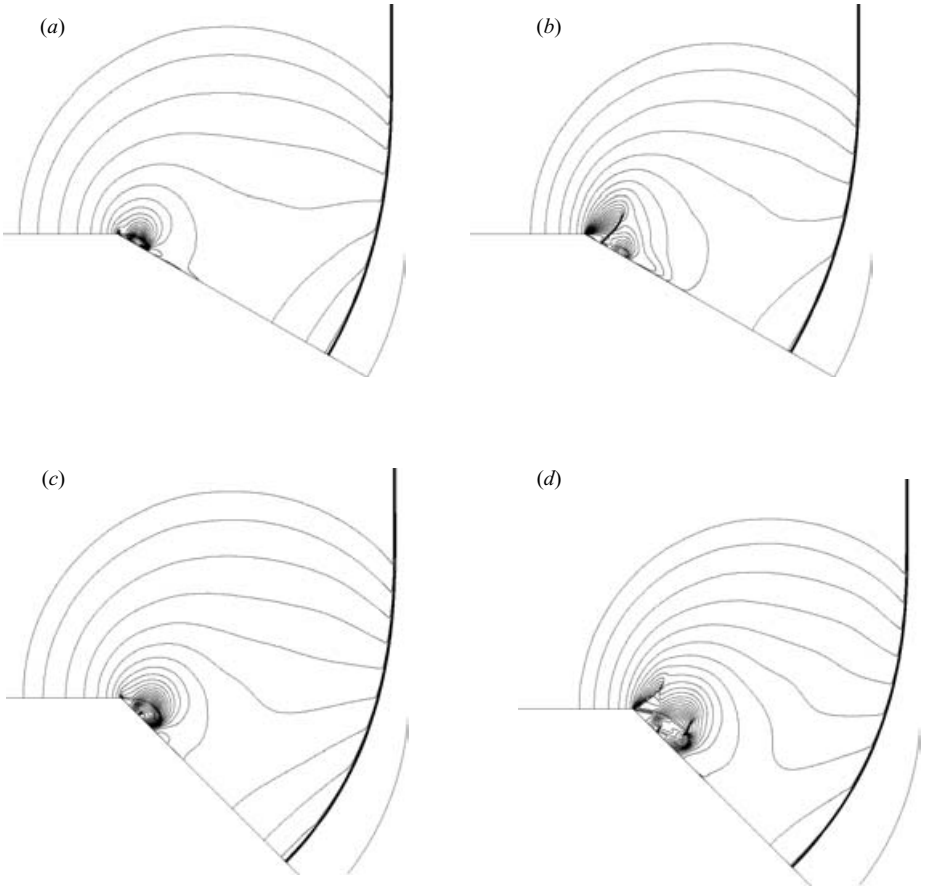

FIGURE 12. Comparison of shock diffraction over 30° and 45° corners: (*a*) $\theta = 30°$, $M_s = 1.4$; (*b*) $\theta = 30°$, $M_s = 1.6$; (*c*) $\theta = 45°$, $M_s = 1.4$; (*d*) $\theta = 45°$, $M_s = 1.6$.

appears near the corners although it spreads wider for the large angle as shown in figure 12(*a*) and 12(*c*). However for $M_s = 1.6$ the flow near the corner turns towards the downstream wall, similar to what happens in the Prandtl–Meyer expansion, and accelerates to a supersonic value. A secondary shock wave then appears on the downstream wall. The slipstream that forms the vortex spiral is no longer visible in figure 12(*b*). The vorticity production is therefore significantly suppressed. For the 60° corner, the slipstream is still seen in figure 12(*d*). This suggests that the slipstream plays an essential role in producing vorticity during shock diffraction.

4.3. *The analytical solution for vorticity production*

For large corner angles, the vortex is produced by the roll-up of the slipstream that is initiated from the corner. If the slipstream is the source of vorticity production, then the rate of vorticity production should be equal to the amount of vorticity entering the flow field along the slipstream in unit time, that is

$$\frac{\Gamma}{t} = \int_{\delta} u\omega \,\mathrm{d}y = \int_{\delta} u \frac{\mathrm{d}u}{\mathrm{d}y} \,\mathrm{d}y = \tfrac{1}{2}U_1^2 - \tfrac{1}{2}U_2^2, \tag{4.1}$$

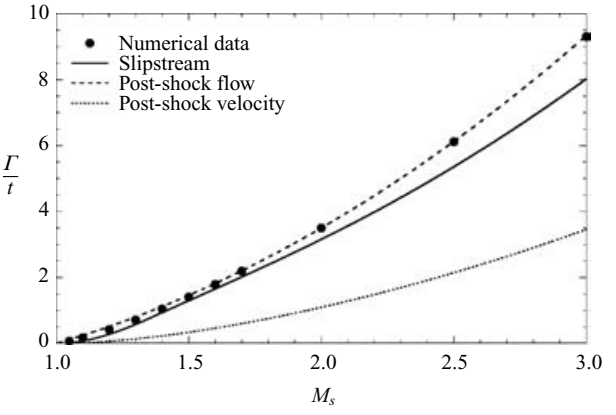

FIGURE 13. Modelling the circulation production over the 180° corner.

A finite thickness δ and a continuous velocity distribution across the slipstream are assumed, so that the mathematical singularity in calculating vorticity $\omega = \partial u/\partial y$ and vorticity flux $u\omega$ is avoided. The rate of vorticity production is just a function of two tangential velocities on each side of the slipstream. Note that the rate depends neither on the thickness nor on the velocity distribution inside the slipstream. In the case of shock diffraction, the velocity below the slipstream but extremely close to the corner satisfies $U_2 = 0$; thus we have a simple relation,

$$\frac{\Gamma}{t} = \tfrac{1}{2}U_1^2. \tag{4.2}$$

In order to evaluate the ratio Γ/t, we should determine the relationship between U_1 and the incident shock Mach number M_s. As a first approximation, U_1 can be taken as the velocity behind the incident shock wave, u_2,

$$\frac{\Gamma}{t} = \tfrac{1}{2}u_2^2. \tag{4.3}$$

This variation is plotted in figure 13 denoted 'Post-shock velocity'. The velocity behind the shock wave is far lower than that above the slipstream, because the flow has experienced a strong expansion at the corner. For example, the flow behind the shock becomes supersonic at $M_s = 2.068$, while the flow above the slipstream is supersonic from $M_s = 1.33$ for large wall angles. To evaluate the velocity U_1, one has to take into account the expansion process during diffraction.

The velocity U_1 is calculated following an analytical model developed by Sun & Takayama (1997) originally for the analysis of the appearance of the secondary shock wave. The corner flow and wave pattern are modelled as shown in figure 14. Regions 1 and 2 correspond to the state in front of and behind the incident shock wave, respectively. The pressure in region 2 is decreased to a lower value in region 3, and the flow is accelerated by the expansion waves, and by the Prandtl–Meyer expansion for strong shock waves. Region 3 designates the state near the convex corner and appears above the slip line. Velocity $U_1 = 1$ in region 3.

For a shock wave behind which the flow is subsonic ($M_s < 2.068$), the reflected expansion wave is generated at the convex corner and its front travels upstream along the solid wall. The pressure p_2 behind the incident shock wave decreases to the

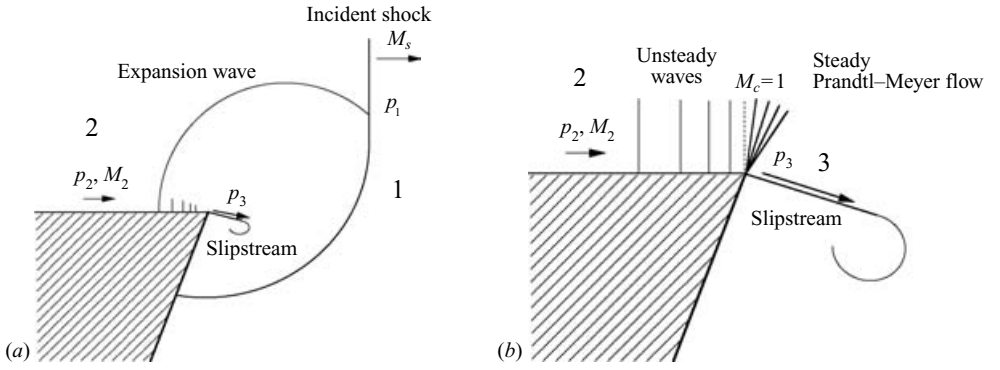

FIGURE 14. Schematic of wave structure in weak shock wave diffraction for analytical modelling; (*b*) is a close-up view of the flow around the corner.

lower pressure at the convex corner p_c so that the local flow Mach number increases to M_c. If M_c is greater than 1, a Prandtl–Meyer flow pattern will be formed at the corner. For a shock wave behind which the flow is supersonic ($M_s > 2.068$), only the Prandtl–Meyer flow pattern will appear.

For $M_s < 2.068$, the unsteady expansion waves should be taken into account. It is noticed that the changes in flow quantities in the direction normal to the upstream wall are negligibly small. This can be seen in photographs shown in figure 6: the fringes on these interferograms appear to be perpendicular to the upstream wall. This fact also suggests that the flow field very close to the upstream wall can be regarded as one-dimensional so that the Riemann invariants are applicable. The following relationship is, therefore, a good approximation for the flow between regions 2 and 3, if $M_c \leqslant 1$:

$$\frac{2a_2}{\gamma - 1} + u_2 = \frac{2a_c}{\gamma - 1} + u_c. \tag{4.4}$$

Denoting $M_c = u_c/a_c$ and $M_2 = u_2/a_2$, gives

$$M_c = M_2 \frac{a_2}{a_c} + \frac{2}{\gamma - 1}\left(\frac{a_2}{a_c} - 1\right), \tag{4.5}$$

where subscript c represents region 3 if the flow in region 3 is subsonic; and it represents flow quantities at $M_c = 1$ if the flow in region 3 is supersonic. For isentropic flow, one has

$$\frac{a_2}{a_c} = \left(\frac{p_2}{p_c}\right)^{(\gamma-1)/2\gamma}. \tag{4.6}$$

Substituting (4.6) into (4.5), one obtains

$$M_c = M_2\left(\frac{p_2}{p_c}\right)^{(\gamma-1)/2\gamma} + \frac{2}{\gamma - 1}\left[\left(\frac{p_2}{p_c}\right)^{(\gamma-1)/2\gamma} - 1\right], \tag{4.7}$$

where M_2 is the flow Mach number behind the incident shock wave and can be readily derived from the normal shock relations for a moving shock wave.

If the pressure p_3 is known, one may replace p_c in (4.7) by p_3, and obtain the value of M_c. If it is less than 1, then $U_1 = M_c a_c$ is obtained by using (4.6) and (4.7). If it is greater than 1, the calculation becomes a little complicated, because

the flow transitions to the Prandtl–Meyer pattern for supersonic flows and unsteady flow formulation (4.7) is not suitable. Since the last characteristic of the left-running expansion wave stays at the corner, the flow Mach number there must be 1. Setting $M_c = 1$ in (4.6) and (4.7), we can calculate pressure p_c and a_c. Using steady isentropic relations that are available in any textbook on gas dynamics, we can readily determine the flow Mach number M_3 and a_3 from the ratio of p_c to p_3, a_c and M_c. The velocity U_1 is then given by $U_1 = M_3 a_3$.

The only unknown in the above analysis is pressure p_3. An approximation is that the final steady flow round the corner will hold with the pressure equal to the initial pressure p_1. Skews (1967) pointed out that, near the wall, the pressure in the slipstream is indeed equal to p_1, although it is lower further away. Sun & Takayama (1997) found that the pressure near the corner is very close to p_1 by numerical calculations, and this trend is much more pronounced for stronger shock waves. Therefore, we adopt

$$p_3 = p_1. \tag{4.8}$$

This approximation is good only for large wall angles. The accuracy of this model has been validated by experiment. It gives M_c starting at 1 for $M_s = 1.346$, which predicts the appearance of the secondary shock wave and agrees very well with experimental data $M_s = 1.33 \pm 0.01$ (Sun & Takayama 1996, 1997).

The rate of circulation production given by this analytical model is summarized in figure 13 denoted 'Slipstream'. The total vorticity in the domain can be estimated by assuming that integral (3.2) contributes to the path that the incident shock wave travels from the corner, if one neglects the velocity change along the upstream and downstream walls. Then one obtains

$$\Gamma = u_2 M_s a_1 t \tag{4.9}$$

or

$$\frac{\Gamma}{t} = u_2 M_s a_1, \tag{4.10}$$

which is also plotted in figure 13 denoted 'Post-shock flow'. It is seen that both models agree fairly well with the numerical data. The post-shock-flow model result is slightly higher than the numerical data for weak shock waves because the flow acceleration along the upstream wall has been neglected, and it agrees excellently with numerical data for strong shock waves. The circulation production given by the slipstream modelling is only slightly below the numerical data, and it always represents a large portion of total vorticity except for very weak shock waves. For example, the slipstream contributes about 92% of total vorticity production for $M_s = 1.5$.

For angles greater than 90°, the rate of circulation production hardly changes with an increase of the angle, and nearly collapses to one curve. A similar tendency has also been observed by Skews (1967) for the angle and velocity of the vortex. A best fit formula for the curve of the 180° corner is, for $M_s \leqslant 1.7$,

$$\frac{\Gamma}{t} = 1.82(M_s - 1) + 1.92(M_s - 1)^2. \tag{4.11}$$

This relation may be used as an approximation for any convex corner with angle larger than 90° since vorticity production does not change much for such large angles. For strong shock waves, (4.10) is a good approximation as shown in figure 13.

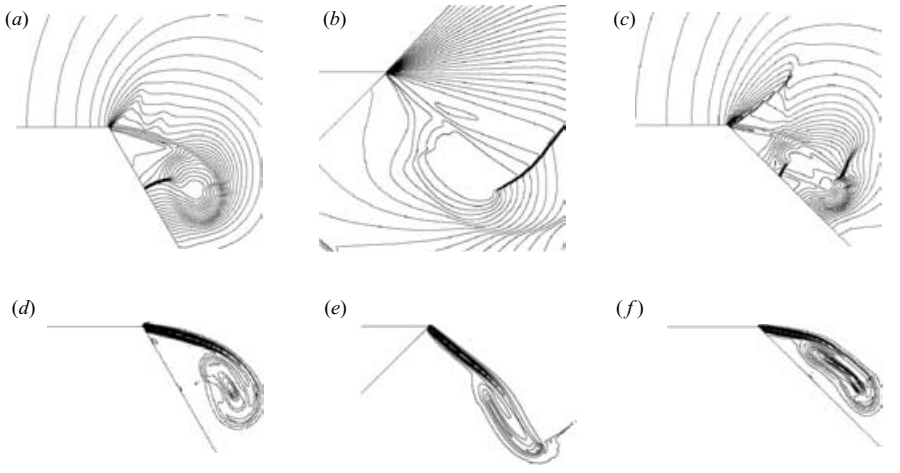

FIGURE 15. Magnified view of corner flows: (*a–c*) density contours, and (*d–f*) vorticity contours. (*a*, *d*), (*b*, *e*) and (*c*, *f*) correspond to figure 7(*d*), figure 9(*d*) and figure 12(*d*), respectively.

4.4. *Some remarks on vorticity production*

For an inviscid compressible flow, the vorticity production equation can be written as, see Bershader (1995),

$$\rho \frac{\mathrm{D}}{\mathrm{D}t}\left(\frac{\omega}{\rho}\right) = (\boldsymbol{\omega}\cdot\nabla)\mathbf{u} + \nabla T \times \nabla s. \tag{4.12}$$

The two terms on the right-hand side are sources for vorticity production. The first term is zero in two-dimensional flows; then it is easily deduced that the second baroclinic term is the dominating source of vorticity. It is common to ascribe the vorticity produced by shock diffraction entirely to baroclinic effects, or the non-isentropic flow behind the curved diffracting shock wave. However, on many interferograms (e.g. figure 6*c–f*), it is seen that a contact surface exists between the main vortex and the diffracted shock wave. Although entropy changes may produce vorticity, the non-isentropic flow behind the diffracted shock wave hardly affects the main vortex that lies on the other side of the contact surface because it is impossible for entropy waves, moving at the speed of the local flow velocity, to pass through the contact surface. Another piece of evidence is that experiments and numerical tests show that the vortex can be greatly suppressed by replacing the sharp corner with a round corner, although the diffracted shock wave is nearly unchanged. These observations suggest that the non-isentropic flows behind the curved shock wave hardly influence the appearance of the main vortex.

In fact, Rott (1956) had already noticed that the main vortex is formed by the rolling up of the slipstream even without considering compressibility. Figure 15 shows a magnified view of the vortex spirals. The contribution of the slipstream to vorticity production is clearly demonstrated by the circulation data for 30° in figure 11, in which vorticity production decreases because of the disappearance of the slipstream. From the analytical modelling of vorticity produced by the slipstream in §4.4, it is further shown that the slipstream contributes to most of the total vorticity.

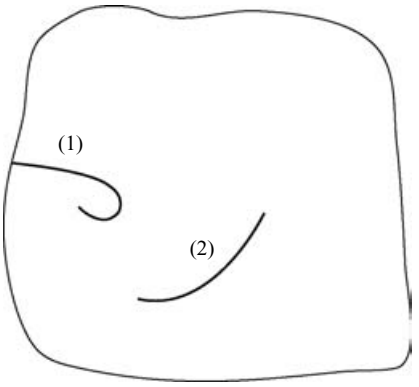

FIGURE 16. Source of vorticity from discontinuities in compressible flows.

The mechanism of vorticity generation from the slipstream is different from the baroclinic effects. One may consider a slipstream without a pressure gradient and with a finite entropy gradient, say a slipstream with a finite thickness, so that the baroclinic term in (4.12) becomes zero. If this slipstream has a tangential velocity jump, it will generate vorticity although the baroclinic term is zero. The slipstream is an independent factor, and sometimes a dominating factor in producing vorticity. This fact is often neglected, or interpreted as a baroclinic effect, when discussing vorticity production.

A sharp corner over a solid boundary is a singular point that may initiate a slipstream and thus produce vorticity. The vorticity production in (4.12) does not include the vorticity that comes from singularities. In compressible flows with shock waves, the slipstream initiating from a sharp corner is not the only source of singularity. Figure 16 sketches two types of singularity that have been observed in experiment. One type (labelled 1) is the slipstream initiated from the boundary of a domain, which is similar to what has been discussed in this paper. The second type of singularity (2) lies within the domain. An example of this singularity is the slipstream initiated from a triple point that appears at the intersection of three shock waves, such as in the case of Mach reflection. Another example is a contact surface with starting and ending point hardly defined, such as those shown in figure 9(*c*, *d*). These singularities are more important sources of vorticity than the baroclinic effects in most unsteady shocked flows, such as in shock–interface interaction (Yang *et al.* 1992, Zabusky & Zeng 1998). This understanding suggests that an efficient way to enhance vorticity production in high-speed flows is to create a slipstream, for instance by generating a Mach reflection.

The slipstream that feeds the main vortex in shock diffraction can be interpreted as the separation of the boundary layer attached to the upstream wall. The slipstream has a finite thickness due to viscosity, and the flow distribution across it is also related to viscosity. The viscosity can also alter the structure of the vortex, especially in the region of the vortex core. However, the amount of vorticity that enters the flow field through the slipstream is determined only by the velocities on both sides of the slipstream, and is hardly influenced by viscosity. If viscosity is taken into account, the rate of circulation production is no longer a constant; it should evolve with time and eventually converge to a constant that agrees with the present inviscid

calculation, that is, the inviscid calculation is the asymptotic solution of the Navier–Stokes equations after a long time evolution during shock diffraction.

5. Summary

Vorticity, in terms of circulation, produced by shock diffraction has been quantitatively calculated by solving the Euler equations, and results and observations are summarized as follows:

(*a*) The rate of vorticity production always increases with wall angle. It increases dramatically in the range from 15° to 45°, and it nearly converges to a constant value for wall angle greater than 90°.

(*b*) The shock strength encourages vorticity production in general for a given wall angle, apart from when the flow experiences a rapid expansion to the downstream wall and suppresses the appearance of the slipstream. A best-fit formula has been provided for large corner angles.

(*c*) An analytical model has been proposed to evaluate the vorticity produced by the slipstream for large wall angles. It is found that the slipstream represents a large portion of the total vorticity. This indicates that a slipstream can be a more dominating factor in producing vorticity in compressible flows than baroclinic effects.

The authors thank the editor and anonymous referees for their valuable comments and help in presenting this work.

REFERENCES

Bershader, D. 1995 Compressible vortices. In *Fluid Vortices* (ed. S. I. Green). Kluwer.

Evans, R. A. & Bloor, M. I. G. 1977 The starting mechanism of wave-inducted flow through a sharp-edged orifice. *J. Fluid Mech.* **82**, 115–128.

Emrich, R. J. & Reichenbach, H. 1969 Photographic study of early stages of vortex formation behind an edge. *Proc. 7th Intl Shock Tube Symposium* (ed. I. I. Glass). University of Toronto Press.

Hillier, R. 1991 Computation of shock wave diffraction at a ninety degrees convex edge. *Shock Waves* **1**, 89–98.

Howard, L. N. & Matthews, J. 1956 On the vortices produced in shock diffraction. *J. Appl. Phys.* **27**, 223–231.

Rott, N. 1956 Diffraction of a weak shock with vortex generation. *J. Fluid Mech.* **1**, 111–128.

Sivier, S., Loth, E., Baum, J. & Löher, R. 1992 Vorticity produced by shock wave diffraction. *Shock Waves* **2**, 31–41.

Skews, B. W. 1967 The perturbed region behind a diffracting shock wave. *J. Fluid Mech.* **29**, 705–719.

Sun, M. 1998 Numerical and experimental studies of shock wave interaction with bodies. PhD thesis, Tohoku University, Japan, http://ceres.ifs.tohoku.ac.jp/~sun/thesis.html.

Sun, M. & Takayama, K. 1996 A holographic interferometric study of shock wave focusing in a circular reflector. *Shock Waves* **6**, 323–336.

Sun, M. & Takayama, K. 1997 The formation of a secondary shock wave behind a shock wave diffracting at a convex corner. *Shock Waves* **7**, 287–295.

Sun, M. & Takayama, K. 1999 Conservative smoothing on an adaptive quadrilateral grid. *J. Comput. Phys.* **150**, 143–180.

Takayama, K. & Inoue, O. 1991 Shock wave diffraction over a 90 degree sharp corner. *Shock Waves* **1**, 301–312.

Toro, E. F. 1999 *Riemann Solvers and Numerical Methods for Fluid Dynamics*, 2nd edn, Springer.

Voinovich, P. A. 1993 Two-dimensional locally adaptive unstructured unsteady Euler code. Advanced Technology Center, St. Petersburg, Russia (unpublished).

White, F. M. 1974 *Viscous Fluid Flow*. McGraw-Hill.

YANG, J. M. 1995 Experimental and theoretical study of weak shock wave. PhD Thesis, Tohoku University, Japan.

YANG, X., CHERN, I.-L., ZABUSKY, N. J., SAMTANEY, R. & HAWLEY, J. F. 1992 Vorticity generation and evolution in shock-accelerated density-stratified interfaces. *Phys. Fluids* A **4**, 1531–1540.

ZABUSKY, N. J. & ZENG, S. M. 1998 Shock cavity implosion morphologies and vortical projectile generation in axisymmetric shock-spherical fast/slow bubble interactions *J. Fluid Mech.* **362**, 327–346.